# The influence of nitrogen doping on the electronic structure of the valence and conduction band in TiO$_2$

Klaudia Wojtaszek,[a] Anna Wach,[a]* Joanna Czapla-Masztafiak,[a] Krzysztof Tyrala,[a] Jacinto Sá,[b,c] Lütfiye Yıldız Özer,[d] Corrado Garlisi,[d] Giovanni Palmisano[d] and Jakub Szlachetko[a]*
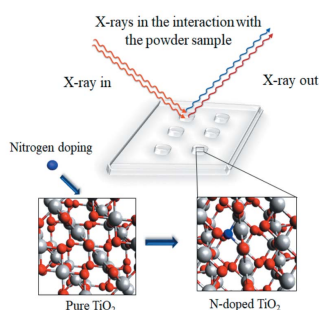
[a]Institute of Nuclear Physics, Polish Academy of Sciences, PL-31342 Krakow, Poland, [b]Department of Chemistry, Uppsala University, Uppsala, Sweden, [c]Institute of Physical Chemistry, Polish Academy of Sciences, Warsaw, Poland, and [d]Department of Chemical Engineering, Khalifa University of Science and Technology, PO Box 54224, Masdar City, Abu Dhabi, United Arab Emirates. *Correspondence e-mail: anna.wach@ifj.edu.pl, jakub.szlachetko@ifj.edu.pl

X-ray emission spectroscopy (XES) and X-ray absorption spectroscopy (XAS) provide a unique opportunity to probe both the highest occupied and the lowest unoccupied states in matter with bulk sensitivity. In this work, a combination of valence-to-core XES and pre-edge XAS techniques are used to determine changes induced in the electronic structure of titanium dioxide doped with nitrogen atoms. Based on the experimental data it is shown that N-doping leads to incorporation of the $p$-states on the occupied electronic site. For the conduction band, a decrease in population of the lowest unoccupied $d$-localized orbitals with respect to the $d$-delocalized orbitals is observed. As confirmed by theoretical calculations, the N $p$-states in TiO$_2$ structure are characterized by higher binding energy than the O $p$-states which gives a smaller value of the band-gap energy for the doped material.

## 1. Introduction

Titanium dioxide, thanks to its unique properties and high number of applications, is the most often studied and used titanium compound in the world. It can make a significant contribution in creating the future-proof solutions for renewable energy sources, environmental protection, chemical industry and medicine. Many technological applications of TiO$_2$ come from photoinduced processes, like photovoltaics, used for producing electric energy from sunlight; photocatalysis, used for pollutants degradation, purification of water, and production of hydrogen; as well as photoinduced superhydrophilicity, used in the formation of anti-fog and self-cleaning surfaces (Carp et al., 2004). Moreover, TiO$_2$ has a high refractive index, which can find application in the production of anti-reflective coatings (Richards, 2004), and a high dielectric constant, which depends on phase and morphology of the material (Wypych et al., 2014) and is utilized in the low-temperature cofired ceramics (LTCC) technology (Pang et al., 2010). Additionally, TiO$_2$ is of particular interest due to the fact that it is chemically and biologically inert, non-toxic, bio- and hemo-compatible with the human body and does not require high production costs (Carp et al., 2004; Schvezov et al., 2010; Ma et al., 2014).

Titanium dioxide is widely recognized as a promising photocatalyst for photo-induced oxidation and reduction reactions. These unique properties of TiO$_2$ were shown for the first time by Fujishima & Honda in 1972 (Fujishima & Honda, 1972). Unfortunately, pure TiO$_2$ has a wide band gap $E_g$



X-rays in the interaction with the powder sample

X-ray in

X-ray out

Nitrogen doping

Pure TiO$_2$       N-doped TiO$_2$

(3.2 eV for the anatase phase and 3.0 eV for the rutile phase) and the photocatalytic reactions are limited to ultraviolet light. Therefore, one of the most important challenges in the photocatalysis field is to modify the electronic structure of the titanium dioxide, especially to reduce the band gap, in order to increase the absorption of visible light (Burda *et al.*, 2003), which constitutes about 45% of the solar energy reaching the Earth's surface. Among various approaches for improving the photocatalytic activity, doping with an appropriately chosen element was successfully employed for $TiO_2$ modification. The best results were achieved in the case of doping with anions of light elements, such as N, C or S, which can cause lower oxidation potential of the doped $TiO_2$ (Charanpahari *et al.*, 2013; Chen & Burda, 2008; Sá *et al.*, 2018).

The improved visible-light absorption and photocatalytic activity of N-doped $TiO_2$ were reported by Asahi *et al.* (2001). The authors calculated the density of states (DOS) using the full-potential linearized augmented plane wave (FLAPW) formalism in the framework of the local density approximation for the substitutional doping with C, N, F, P and S to replace oxygen atoms in the $TiO_2$ anatase phase. Additionally, they also compared the calculated DOS for pure anatase and anatase doped with nitrogen at different sites: substitutional, interstitial and simultaneous substitutional and interstitial. It was shown that the substitutional N-doping of $TiO_2$ is the most effective due to the contribution of nitrogen *p*-states in narrowing the band gap by mixing with O 2*p* states. In this context, it is noteworthy to mention that the authors took into account three very important assumptions regarding the effectiveness of photocatalysts. Firstly, the size of the band gap of the photocatalyst has to allow activation by visible light. Secondly, the $TiO_2$ conductivity band has to be above the $H^+/H_2$ reaction potential of the standard electrode and the valence band below the $O_2/H_2O$ reaction potential. Thirdly, the transport time of charge carriers to the surface of the photocatalyst has to be shorter than their lifetime. In addition to theoretical calculation, the authors evaluated optical properties and photocatalytic activity of N-doped $TiO_2$. In particular, the photodecomposition of methylene blue and gaseous acetaldehyde, as well as the photoinduced hydrophilicity of the foil's surface under visible light (wavelength < 500 nm), was investigated. These studies were combined with measurements of the N 1*s* core-level spectra by means of X-ray photoelectron spectroscopy (XPS). The obtained results showed an increase of the photocatalytic activity along with an increase of the N component peak at 396 eV, the position of which is consistent with the value attributed to the atomic *β*-N state in $TiO_{2-x}N_x$. Moreover, the optimal nitrogen content was found, above which a significant decrease in the photocatalytic activity is observed. This phenomenon might be explained by changes in the crystal structure of the sample caused by the high nitrogen doping.

In the following years, several similar experimental and theoretical works were conducted (Sakthivel *et al.*, 2004; Sathish *et al.*, 2005; Sato *et al.*, 2005; Di Valentin *et al.*, 2005; Wang *et al.*, 2015). The main differences between them are in the sample preparation method, the type of the sample (powder samples, thin films, nanotubes), characterization methods (mainly XRD, XPS, TEM, HRTEM, optical absorption spectroscopy, photocatalytic activity measurements) or calculation formalism (DFT, FLAPW, FEFF). Invariably, these studies confirmed that doping of $TiO_2$ with nitrogen atoms increases the absorption of visible light. Nevertheless, more profound research showed that, with increasing N dopant content, the photocatalytic quantum yield decreases (Irie *et al.*, 2003; Wang *et al.*, 2009) despite the higher visible-light absorption. This effect was explained by the formation of additional $Ti^{3+}$ sites and associated with them oxygen vacancies, which act as recombination places for the photoinduced electron–hole pairs. Their presence leads to a decrease in overall photocatalytic activity.

In order to gain insight into the electronic structure of nitrogen-$TiO_2$ nanoparticles, Chen *et al.* (2010) employed X-ray absorption and X-ray emission spectroscopy (XAS and XES). They showed that the measured O 1*s* XAS and XES spectra are almost identical for pure and N-doped $TiO_2$. On the other hand, slight differences in the intensity of peaks were observed in Ti 2*p* spectra. This is explained by differences between O 2*p* and N 2*p* orbitals coupling with Ti 3*d* orbitals in the conduction band. Therefore, the authors acknowledged that only Ti states were modified during nitrogen doping. It was also suggested that the nitrogen atoms replace oxygen in the $TiO_2$ lattice and the substitution does not cause any significant change in the crystal field. In addition, N 1*s* XAS spectra confirmed the formation of N—Ti bonds in the studied nanoparticles and the contribution of nitrogen in the electronic structure of N-doped $TiO_2$. Simultaneously, the possibility of nitrogen interstitial doping was excluded.

Parks Cheney *et al.* (2014) investigated the cause of band gap reduction ($\sim 1$ eV) in Cr/N co-doped rutile $TiO_2$ by means of soft X-ray spectroscopy. They showed that the reduction of the band gap originates for two main reasons: (i) formation of Cr $3d^3$ levels in the lower half of the band gap and (ii) contribution of localized Cr 3*d* states and delocalized N 2*p* states in the conduction band minimum. The experimental data in combination with theoretical calculations of the density of electron states for Cr-doped anatase $TiO_2$ were presented by Wojtaszek *et al.* (2016). The authors used resonant X-ray emission spectroscopy (RXES) to probe the electronic states. It was shown that the chromium doping induces an additional electronic band on the low-energy side of the conduction band. More importantly, the data obtained by the RXES method allowed the impact of doping on localized and delocalized *d*-orbitals to be distinguished.

In the present work, we apply a combined valence-to-core XES, XAS and theoretical simulations to study changes in electronic states around the Fermi energy for a recently developed (Ozer *et al.*, 2017) N-doped $TiO_2$ nanoparticle grown on reduced graphene oxide. Use of hard X-ray spectroscopy allowed probing the material in non-vacuum conditions (ambient environment) and with bulk sensitivity (>1 µm). We demonstrate that N 2*p* states are responsible for the reduction of the band gap in N-doped $TiO_2$ grown on

reduced graphene oxide and thus leading to an increase in visible range absorption. Simultaneously, the XAS reveals the decrease in the population of unoccupied $d$-localized orbitals with respect to unoccupied delocalized $d$-states. This work confirms high sensitivity of the employed experimental methods for high-detail determination of electronic states around the Fermi energy with bulk sensitivity and out-of-vacuum conditions.

## 2. Experimental section

The nitrogen-doped $TiO_2$ nanoparticles were grown on reduced graphene oxide sheets via the sol-gel route, according to the procedure reported previously (Ozer *et al.*, 2017). Briefly, titanium (IV) butoxide (TBOT), 2-propanol and hydrochloric acid (4 $M$) were mixed in a volumetric ratio of 1:5.461:1.283, respectively. Reduced graphene oxide [fixed at 1% ($w/w$) with respect to $TiO_2$] and ammonium nitrate, used as the N-doping agent [0.8% ($w/w$)], were dispersed/dissolved in the water prior to mixing with TBOT, HCl and 2-propanol solution. The resulting mixture was kept under stirring at 70°C for 20 h. Afterwards, the product was dried by means of the rotary evaporator at 70°C. Finally, the sample was thermally treated under nitrogen flow at 450°C for 4 h.

The experimental data were obtained at the SuperXAS beamline at the Swiss Light Source synchrotron in Villigen, Switzerland. The beamline is dedicated to XAS and XES measurements, which are characterized by high sensitivity and time resolution (Szlachetko *et al.*, 2013, 2014*a*). The experiment was conducted with X-ray energies around the $K$-absorption edge of Ti (4966 eV) using a double-crystal Si(111) monochromator. The X-ray spot size on the sample was 100 μm × 100 μm with a photon flux of $10^{11}$ photons s$^{-1}$.

A von Hamos-type wavelength-dispersive X-ray spectrometer was chosen for valence-to-core XES spectra measurements. The spectrometer was equipped with a segmented silicon diffraction crystal with a relatively small radius of curvature (25 cm). In particular, a Si(400) diffraction crystal was employed, which provides a Bragg angle of about 66°. This experimental setup allows a high-energy resolution detection of about 300 meV to be obtained and relatively high detection efficiency without using scanning elements (Szlachetko *et al.*, 2012). A Pilatus 2D detector with a pixel size of 175 μm × 175 μm detected the X-rays diffracted on the Si(400) crystal. These properties enable high sensitivity and short acquisition times (of the order of a few or tens of seconds), making this setup an ideal

solution for experiments where the composition and properties of the sample or other measurement conditions may change during the experiment. The non-resonant valence-to-core XES spectra were recorded at an incident beam energy of 100 eV above the $K$-ionization threshold (*i.e.* 5066 eV). The energy calibration of the spectrometer setup was performed with elastically scattered photons with energy tuned around the valence-to-core transition. Finally, the XES measurements were complemented with XAS. X-ray absorption spectra around the Ti $K$-edge were measured in the fluorescence mode using a four-element SDD detector. The experimental geometry was identical for all studied samples.

The obtained experimental data were also compared with theoretical calculations of the DOS performed with the *FEFF9.0* program. For calculations, we used $TiO_2$ rutile structure and assumed substitutional replacement of O atoms by N atoms. It is important to note that the obtained N-doped $TiO_2$ was a mixture of brookite and rutile crystal phase; however, negligible changes in the calculated DOS between these two phases were observed. In particular, the calculations were performed for a 1 nm particle with the N atom placed at a first coordination shell in a crystal structure of rutile [Fig. 1(*a*)]. We simulated that doping at the second shell has no influence on the electronic structure of the scattering central
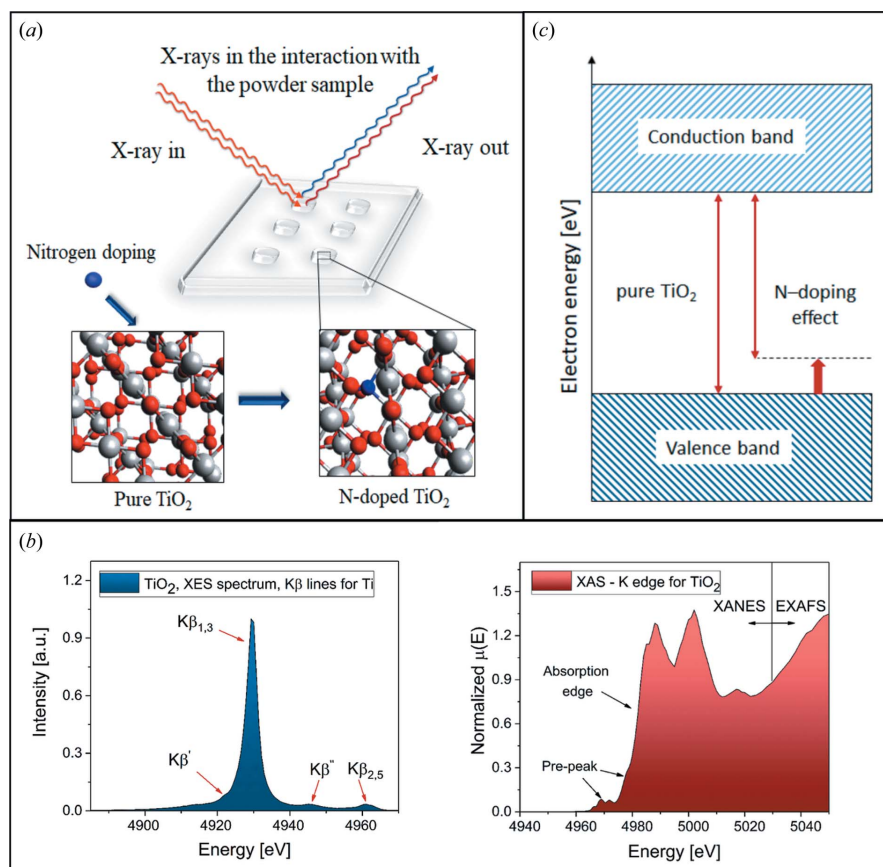


**Figure 1**
Experimental concept (*a*) and measured emission and absorption X-ray spectra for pure $TiO_2$ with marked spectral structures (*b*) as well as the sense and current information on doping the rutile phase with nitrogen atoms (*c*).

Ti atom. In calculations, we used the Hedin–Lundqvist energy-dependent exchange-correlation potential method for fine structure and atomic background.

## 3. Results and discussion

The scheme depicting the concept of the experiment is presented in Fig. 1(a). The experiment aims at measuring two spectroscopy signals: X-ray emission and X-ray absorption. The X-ray emission signal is measured at a fixed X-ray energy above the ionization threshold. On the other hand, the X-ray absorption is obtained by recording the total fluorescence signal while scanning the incidence X-ray energy across the ionization threshold. The measured XES and XAS spectra for the pure $TiO_2$ sample are plotted in Fig. 1(b) in blue and red, respectively.

As marked in Fig. 1(b), the electronic transitions corresponding to emission lines in the XES spectrum are the 'core-to-core' and 'valence-to-core' transition types denoted by four types of $K\beta$ emission lines. The main lines, namely $K\beta'$ and $K\beta_{1,3}$, represent the core-to-core transitions from the $3p$ state to the $1s$ state. Their energy separation is caused by the exchange interaction of the electronic $3p$ states with the occupied $3d$ states of titanium. Simultaneously, the $K\beta''$ and $K\beta_{2,5}$ lines correspond to the transition of electrons from the valence shells of elements to the $1s$ state. The spectral shape and peaks positions provide information about the density of the occupied electron states in the scattering element. Fig. 1(b) also shows the absorption spectrum for the Ti K-edge. For the purpose of the present study, we focus on pre-edge features located in the energy range 4965–4975 eV. In the pre-edge structure of $TiO_2$, we can distinguish four pre-peaks resulting from $s$–$d$ type quadrupole transitions, which in the titanium dioxide compound are characterized by a high occurrence probability due to the hybridization of the $d$ and $p$ states. The peaks are located at energies of 4966.4 eV, 4968.86 eV,

4971.88 eV and 4978.12 eV. According to the literature (Caliebe et al., 1998; Glatzel et al., 2009; Pramod et al., 2014; Szlachetko & Sá, 2014), the first pre-edge peak corresponds to the transition from the $1s$ state to the localized $3d$ states of titanium. The second and third peaks are attributed to transitions from the $1s$ state to the delocalized $3d$ states of titanium, which are additionally partially hybridized with the $p$ states of oxygen atoms surrounding the titanium. The fourth peak, which is energetically localized on the absorption edge, is a result of the transitions from the $1s$ to $4p$ states of titanium. These structures are very important due to their participation in the creation of the minimum conduction band as well as their impact on the band gap. Therefore, they provide information about the density of unoccupied states in the studied element.

In this work, the measured valence-to-core X-ray emission and pre-edge X-ray absorption spectra are plotted in Fig. 2(a) in order to compare the electronic structure of the conduction and valence band of N-doped $TiO_2$-grown on reduced graphene oxide at the level of 1% and the reference, pure $TiO_2$ in the brookite-rutile phase. In the previous study, it was noticed that the effect of reduced graphene oxide on the band gap is negligible; thus, we focus on the band gap tuning effect of nitrogen doping (Ozer et al., 2017).

The combination of XES and XAS measurements enables the electronic band structure of occupied and unoccupied states, respectively, to be mapped. By tuning the X-ray energy close to the $1s$ ionization threshold of Ti, the core-electron is excited above the Fermi level to an unoccupied state. Subsequently, this intermediate excited state decays radiatively with simultaneous emission of an X-ray photon. The decay transition may involve either another core-electron or a valence electron from a higher occupied orbital. By measuring the intensity of the incidence and emitted X-rays the conduction and valence states are probed in a single scattering process. Furthermore, due to the involvement of the $s$-type core-state
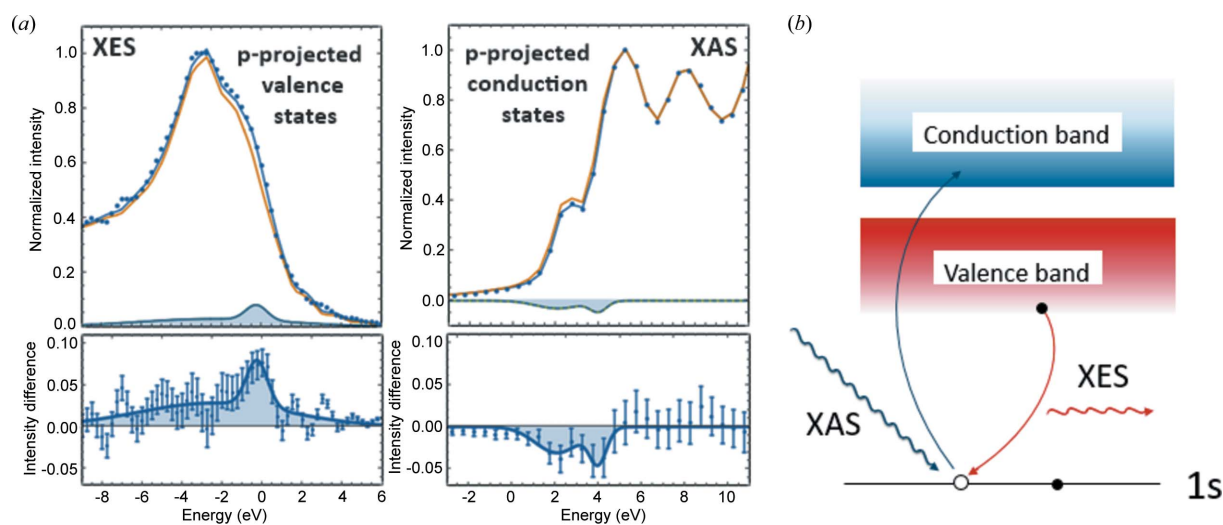


**Figure 2**
Measured XES and XAS spectra for un-doped (orange line) and N-doped (blue points) samples with spectral changes (blue line) induced by nitrogen doping and error estimates of the measured data points (a). Schematic representation of the X-ray scattering process used for mapping the electronic band structure (b).

the mapped density of states is *p*-projected, *i.e.* determined by means of dipole selection rules. Fig. 2(*b*) illustrates the process described above. It is important to note that the application of X-ray absorption and X-ray emission spectroscopies provides a bulk sensitivity, which implies that the core-hole states are used to map valence and conduction bands. For this reason, the core-hole lifetime and hence state-width is imposed on the measured spectral features. In the presented Ti *K*-edge experiment, the 1*s* initial core-hole broadening, that is used to map valence and conduction bands, is equal to 0.9 eV (Campbell & Papp, 2001). This broadening is additionally combined with an experimental resolution of 1.1 eV. As a consequence, the measured spectra exhibit tails extending towards the low- and high-energy side, leading to an overlapping effect of neighbouring electronic states (*e.g.* valence versus conduction).

For data interpretation, the measured XES and XAS spectra for un-doped (orange line) and N-doped (blue points) samples are plotted in Fig. 2(*a*). Comparison of the spectra reveals a shift of the XES signal and an intensity decrease in the pre-edge feature of the XAS curves. The energy scale of the spectra was re-calibrated to around the Fermi energy by subtracting a value of 4963.8 eV that corresponds to an inflection point of the high-energy side of the valence states. Moreover, the spectra were background-subtracted using a linear function as a background model. The same procedure was employed for doped and un-doped samples to ensure that no signal effects are introduced with background subtraction analysis. Finally, the spectra were normalized in the 0 to 1 range for comparison purposes. In order to qualitatively analyse the obtained results, a linear combination fit procedure was employed on the N-doped spectra. In the procedure we used un-doped $TiO_2$ spectra as reference and a parameter-free Gaussian function in order to account for new spectral features for the N-doped sample. Indeed, the analysis showed that two Gaussian functions have to be employed for the fitting procedure in both XES and XAS signals. The result of the fitting procedure is compared with measured data, shown as the blue solid line in Fig. 2(*a*). The analysis reveals that the signal changes on the valence electronic side correspond to a new electronic band introduced at the high-energy side of the valence states. This band is represented by a Gauss profile fitted to the signal with a nominal centre position at −0.2 eV and width of 1.3 eV (full width at half-maximum). This feature is accompanied by a weak and broad structure, positioned at −2.5 eV and with 9.0 eV width. Determined Gaussian profiles with error estimates of the measured data points are presented in the bottom panel of Fig. 2(*a*). The same procedure was also applied to analyse electronic structure changes of the conduction band with the XAS spectrum, employing a reference spectrum of un-doped Ti sample and parameter-free Gaussian functions. Unlike the XES spectrum, the XAS signal shows an intensity drop at the lowest electronic states positions that are interpreted as the *d*-localized $TiO_2$ band (Szlachetko & Sá, 2014; Szlachetko *et al.*, 2014*b*). The data reveal that N-doping decreases the population of the *d*-localized orbital. Moreover, the fitting procedure identifies two

distinctive energies at which the spectral changes are observed, namely at 2.1 eV and 4.0 eV with respect to the Fermi energy. The comparison between determined profiles and difference of experimental data shows a proper approximation of the signal difference within the statistical error of the measured data points. Finally, the fitting procedure allowed for quantitative analysis indicating that the amount of un-affected Ti sites for doped samples equals 98.6% (for XES) and 99.0% (for XAS), *i.e.* in good agreement with the expected 1% N doping level.

In addition to experimental data, theoretical calculations were conducted in order to assign experimental features and deconvolute contributions of different atomic orbitals. The calculations of the DOS were performed using the *FEFF9.0* program. The calculated data for the *s*, *p* and *d* states of titanium and the *s* and *p* states of oxygen as well as nitrogen are shown in Fig. 3.

Based on theoretical calculations and the shape of the experimental spectra, it can be concluded that the $TiO_2$ valence band is composed of the 3*d* titanium states and the 2*p* oxygen states. The observation suggests that these are hybrid states, because they partially overlap in the energy scale. Furthermore, the 3*d* states of titanium and the 2*p* states of oxygen form a single structure as observed in the experimental spectrum. At a lower relative emission energy of −18.1 eV, a second structure is observed, which is related to a transition from the 2*s* oxygen state to the 1*s* state of titanium. This transition is possible due to partial hybridization of the 2*s* oxygen states with the *d*-states of titanium. In the case of the conduction band, we can conclude that it is mainly composed of the unoccupied 3*d* Ti orbitals. Moreover, the oxygen
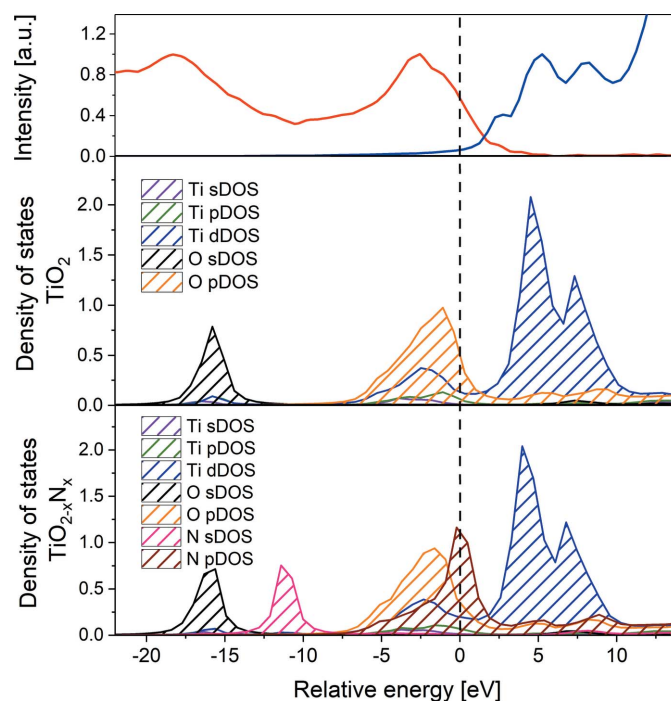


**Figure 3**
The density of electronic states for pure and substitutional N-doped $TiO_2$.

contribution in the formation of the band is insignificant. The conductivity states have a heterogeneous structure, consisting of three structures composed of the Ti $d$-band in the relative energy range 1.5–9.8 eV. Incorporation of an N atom into the $TiO_2$ structure gives two new electronic bands below the Fermi level. Firstly, the 2$s$ N orbital is observed at a higher energy of about 5 eV than the 2$s$ orbital of oxygen. Considering that these orbitals are too deep in energy, they do not contribute to the valence states and thus do not play any crucial role in the photocatalytic properties of the material. Secondly, the nitrogen doping results in the appearance of 2$p$ orbitals of N at higher energy (of about 2 eV) with respect to the 2$p$ orbital of oxygen. Calculations agree with the experimental results and confirm the shift of the valence band and narrowing of the material band gap energy. On the conduction-band site, the influence of N doping is negligible and new features are not observed.

It is noteworthy that the calculated DOS are in general accordance with results shown by Asahi *et al.* (2001). Asahi *et al.*'s DOS calculations proved that substitutional nitrogen-doping of $TiO_2$ is most effective in narrowing the band gap due to the mixing of nitrogen $p$-states with O 2$p$ states. This is also in line with results presented by Zhao & Liu (2008). They calculated the DOS by using density functional theory to compare the anatase $TiO_2$ structure with substitutional nitrogen, interstitial nitrogen or oxygen vacancy induced by N doping. On the other hand, Chen & Dawson (2015) performed their research assuming different nitrogen substitution sites in $TiO_2$. As a result, the calculated DOS relates to nitrogen substitution at a Ti site and formation of nitrite or nitrate molecules. We cannot confirm this effect (*i.e.* substitutional replacement of Ti and N atoms) in our experimental data. Indeed, the obtained spectral difference confirms the theoretical predictions of Asahi *et al.* as well as those of Zhao *et al.* that consider substitutional or interstitial replacement of O atoms by nitrogen or interstitial N doping at an O vacancy. In conclusion, the obtained results confirm that the doped material fulfils the second condition given by Asahi *et al.* (2001) for the electrical potential of the band located above the $H^+/H_2$ reaction potential of the standard electrode. As previously stated, the condition is necessary for the occurrence of redox reactions on the surface of the photocatalyst.

## 4. Conclusions

In summary, a combination of valence-to-core XES and pre-edge XAS measurements at synchrotron light sources with theoretical calculations (DOS simulations) enabled determination of the electronic structure of N-doped $TiO_2$ nanoparticles grown on reduced graphene oxide. It was found that N-doping markedly affects the occupied electronic side, leading to band gap narrowing. From an electronic point of view, the smaller band gap of a doped semiconductor might not only improve visible light uptake but also the photocatalytic performance.

## References

Asahi, R., Morikawa, T., Ohwaki, T., Aoki, K. & Taga, Y. (2001). *Science*, **293**, 269–271.
Burda, C., Lou, Y., Chen, X., Samia, A. C. S., Stout, J. & Gole, J. L. (2003). *Nano Lett.* **3**, 1049–1051.
Caliebe, W. A., Kao, C.-C., Hastings, J. B., Taguchi, M., Kotani, A., Uozumi, T. & de Groot, F. M. F. (1998). *Phys. Rev. B*, **58**, 13452–13458.
Campbell, J. L. & Papp, T. (2001). *At. Data Nucl. Data Tables*, **77**, 1–56.
Carp, O., Huisman, C. L. & Reller, A. (2004). *Prog. Solid State Chem.* **32**, 33–177.
Charanpahari, A., Umare, S. S. & Sasikala, R. (2013). *Appl. Surf. Sci.* **282**, 408–414.
Chen, H. & Dawson, J. A. (2015). *J. Phys. Chem. C*, **119**, 15890–15895.
Chen, X. & Burda, C. (2008). *J. Am. Chem. Soc.* **130**, 5018–5019.
Chen, X., Burda, C., Guo, J., Smith, K. E., Glans, P.-A. & Learmonth, T. (2010). *Arab. J. Sci. Eng.* **35**, 65–71.
Di Valentin, C., Pacchioni, G., Selloni, A., Livraghi, S. & Giamello, E. (2005). *J. Phys. Chem. B*, **109**, 11414–11419.
Fujishima, A. & Honda, K. (1972). *Nature*, **238**, 37–38.
Glatzel, P., Sikora, M. & Fernández-García, M. (2009). *Eur. Phys. J. Spec. Top.* **169**, 207–214.
Irie, H., Watanabe, Y. & Hashimoto, K. (2003). *J. Phys. Chem. B*, **107**, 5483–5486.
Ma, Y., Wang, X., Jia, Y., Chen, X., Han, H. & Li, C. (2014). *Chem. Rev.* **114**, 9987–10043.
Ozer, L. Y., Shin, Y., Felten, A., Oladipo, H., Pikuda, O., Muryn, C., Casiraghi, C. & Palmisano, G. (2017). *J. Environ. Chem. Eng.* **5**, 5091–5098.
Pang, L.-X., Wang, H., Zhou, D. & Yao, X. (2010). *J. Mater. Sci. Mater. Electron.* **21**, 1285–1292.
Parks Cheney, C., Vilmercati, P., Martin, E. W., Chiodi, M., Gavioli, L., Regmi, M., Eres, G., Callcott, T. A., Weitering, H. H. & Mannella, N. (2014). *Phys. Rev. Lett.* **112**, 036404.
Pramod, C. V., Raghavendra, C., Reddy, K. H. P., Babu, G. V. R., Rao, K. S. R. & Raju, B. D. (2014). *J. Chem. Sci.* **126**, 311–317.
Richards, B. S. (2004). *Prog. Photovolt. Res. Appl.* **12**, 253–281.
Sá, J., Garlisi, C., Palmisano, G., Czapla-Masztafiak, J., Kayser, Y. & Szlachetko, J. (2018). *Mater. Chem. Phys.* **208**, 281–288.
Sakthivel, S., Janczarek, M. & Kisch, H. (2004). *J. Phys. Chem. B*, **108**, 19384–19387.
Sathish, M., Viswanathan, B., Viswanath, R. P. & Gopinath, C. S. (2005). *Chem. Mater.* **17**, 6349–6353.
Sato, S., Nakamura, R. & Abe, S. (2005). *Appl. Catal. Gen.* **284**, 131–137.
Schvezov, C. E., Alterach, M. A., Vera, M. L., Rosenberger, M. R. & Ares, A. E. (2010). *JOM*, **62**, 84–87.
Szlachetko, J., Ferri, D., Marchionni, V., Kambolis, A., Safonova, O. V., Milne, C. J., Kröcher, O., Nachtegaal, M. & Sá, J. (2013). *J. Am. Chem. Soc.* **135**, 19071–19074.
Szlachetko, J., Michalow-Mauke, K., Nachtegaal, M. & SÁ, J. (2014*b*). *J. Chem. Sci.* **126**, 511–515.
Szlachetko, J., Nachtegaal, M., de Boni, E., Willimann, M., Safonova, O., Sá, J., Smolentsev, G., Szlachetko, M., van Bokhoven, J. A., Dousse, J., Hoszowska, J., Kayser, Y., Jagodzinski, P., Bergamaschi, A., Schmitt, B., David, C. & Lücke, A. (2012). *Rev. Sci. Instrum.* **83**, 103105.
Szlachetko, J. & Sá, J. (2014). *CrystEngComm*, **15**, 2583–2587.

Szlachetko, J., Sá, J., Nachtegaal, M., Hartfelder, U., Dousse, J.-C., Hoszowska, J., Abreu Fernandes, D. L., Shi, H. & Stampfl, C. (2014a). *J. Phys. Chem. Lett.* **5**, 80–84.

Wang, J., Tafen, de N., Lewis, J. P., Hong, Z., Manivannan, A., Zhi, M., Li, M. & Wu, N. (2009). *J. Am. Chem. Soc.* **131**, 12290–12297.

Wang, J., Zhao, Y. F., Wang, T., Li, H. & Li, C. (2015). *Physica B*, **478**, 6–11.

Wojtaszek, K., Tyrala, K., Czapla-Masztafiak, J., Sá, J. & Szlachetko, J. (2016). *Chem. Phys. Lett.* **664**, 73–76.

Wypych, A., Bobowska, I., Tracz, M., Opasinska, A., Kadlubowski, S., Krzywania-Kaliszewska, A., Grobelny, J. & Wojciechowski, P. (2014). *J. Nanomater.* **2014**, 1–9.

Zhao, Z. & Liu, Q. (2008). *J. Phys. D Appl. Phys.* **41**, 025105–025115.